# THE DISTRIBUTION AND MOTION OF AIR BUBBLES
# IN THE WAKES OF STEADY BREAKING WAVES

**J. H. Duncan, C. Y. Li, M. P. Miller, and X. Liu**
Department of Mechanical Engineering
University of Maryland
College Park, MD 20742

## ABSTRACT

Experimental measurements of the two-phase flow in two steady breaking waves with the same phase speed but different breaking intensities are presented. The measurements include the mean and root-mean-square surface height profiles of the breakers; the vertical distributions of mean horizontal velocity in the wakes; and the radii, spatial distributions, and velocities of the bubbles in the wakes. At positions ranging from 0.6 to 1.0 gravity wavelengths behind the breaker, the vertical distributions of void fraction are near zero at the free surface, reach peaks at depths between 10 and 20 mm below the free surface and tend to zero at larger depths. The bubbles move downstream in the reference frame of the wave and rise vertically at speeds that are less than that of a bubble of the same size rising in a quiescent fluid. Near the surface, the mean horizontal water and bubble velocities are equal, but in the wake shear layer the bubbles move more slowly than the water. The void fractions for the stronger breaker are larger than those for the weaker breaker.

## 1. INTRODUCTION

Over a wide range of operating conditions, breaking waves are found near the bow and downstream of the stern of ships moving in calm water. Air bubbles are entrained by these breakers and some of the bubbles are left behind the breaker embedded in a turbulent surface wake. These two-phase wakes are of practical interest because some the bubbles entrained by the waves in the forward part of the ship flow field may migrate to the propeller where they act as cavitation nuclei and because of the possibility of ship detection via the trail of bubbles left behind.

For a wide range of operating conditions, the sections of the breaking wave crests far from the ship's track appear as steady spilling breakers. In order to explore the dynamics of these breakers, a number of investigators have examined two-dimensional breakers generated by a hydrofoil moving near a free surface at constant speed, depth, and angle of attack. Battjes and Sakai (1981) measured the flow field behind the breaker and found a turbulent wake at the free surface. It has been shown by Duncan (1981 and 1983) that the momentum deficits in these wakes are caused by the shear stress of the turbulent air-water mixture (called the breaking region) that rides on the forward face of the wave. Casual observations of these laboratory-scale flows indicated that, as in the breakers produced by ships, bubbles from the breaking region travel into the wake and eventually rise to the water surface downstream.

The behavior of small bubbles rising in a quiescent fluid has been studied experimentally by many authors (see the review by Harper (1972) and the recent measurements of Maxworthy et al. (1996)). In clean water at room temperature, the bubble rise velocity increases as the bubble radius increases and reaches a maximum of about 35 cm/s at a radius of about 0.7 mm. As the bubble radius is increased further, the rise velocity initially decreases. Bubbles with diameters of about 1 mm rising in pure water with a homogeneous turbulent background have been studied using numerical simulations by Spelt and Biesheuvel (1997). They found that the turbulence reduces the rise velocity by as much as 60% from its value in a quiescent fluid. Experimental measurements of bubble behavior in a turbulent flow generated in a vertical water tunnel with an active grid have been reported by Poorte (1998). The experimental results are in agreement with the predictions of Spelt and Biesheuvel (1997) for weak turbulence.

In the present study, some aspects of the two-phase flow in hydrofoil-produced breakers are studied experimentally. The experiments were performed in a towing tank that is 14.8 m long, 1.2 m wide and 1.0 m deep (see Figure 1). A NACA 0012 hydrofoil with a 20-cm chord was used to generate the breakers. The foil was operated at one speed, one angle of attack and two depths of submergence. In this manner, two breakers with the same phase speed but different breaking intensities were produced. Three types of measurements were made: the mean and root-mean-square fluctuation of the breaking wave crest profiles were measured with a pho-
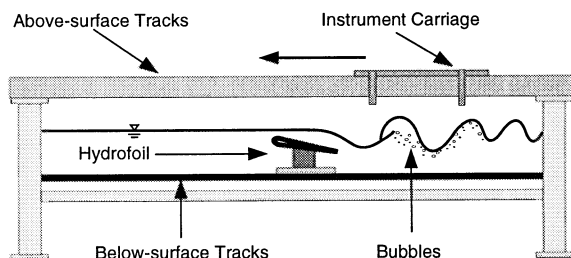
Figure 1. Schematic showing wave tank, instrument carriage and hydrofoil.

tographic technique that employs laser-induced fluorescence; the vertical distributions of mean horizontal velocity in the wakes were measured with Pitot tubes; and the spatial distributions, sizes and velocities of bubbles in the wake were measured with a shadowgraph method.

The remainder of this paper is divided into three sections. Descriptions of the wave tank, hydrofoil and measurement techniques are given in Section 2. The experimental results are presented and discussed in Section 3. Finally, the conclusions are given in Section 4.

## 2. EXPERIMENTAL DETAILS
### 2.1 Wave tank

The experiments were performed in a towing tank with dimensions of 14.8 m long, 1.22 m wide and 1.0 m deep, see Figure 1. The side walls of the tank are made of glass to allow for flow visualization and optical measurements. The tank contains both below-surface and above-surface towing systems. The below-surface towing system includes two fully submerged 'L'-shaped tracks that are mounted from the bottom of the tank near each of the long side walls. Objects are towed along the tracks by two stainless steel wire ropes which enter the water at one end of the tank and leave from the other end. Thus, no part of the towing system breaks the water surface in the vicinity of the towed object. The wire ropes are driven by a servo motor mounted at one end of the tank. The above-surface towing system uses two tracks mounted above the tank, one near each sidewall. The above-surface towing system includes an instrument carriage that rides on the tracks via four hydrostatic oil bearings. When high-pressure oil is supplied to the bearings, a thin film of oil is forced between the bearings and the tracks, thereby greatly reducing vibration and friction levels of the carriage. The carriage is driven by two separate wire ropes that are powered by the same servo motor that powers the below-surface towing system. With this system, the instrument carriage and the hydrofoil (described below) move along the tank at the same speed. The relative position between the foil and the carriage can be varied over a wide range. Precise towing speeds are obtained by means of a computer-based feedback control system. The towing speed is verified with an independent measurement obtained from two timing switches located 209.9$cm$ apart and connected to a timer with nanosecond accuracy.

In the present experiments, breaking waves were generated with a hydrofoil mounted to the below-surface towing

system. The hydrofoil is an aluminum NACA-0012 airfoil with a 20-cm chord. The foil spans the width of the tank with a small clearance between the edges of the foil and the walls of the tank. The foil is mounted to two stainless steel plates which, in turn, are mounted to two Delrin blocks. Each Delrin block has a groove cut into it; these grooves provide a low friction bearing surface to slide along the submerged L-shaped tracks.

In order to control water clarity and surfactants, a recirculating skimmer system was used. This system includes two surface skimmers located at one end of the tank. The water from the skimmers was sent through an ozonator into a large holding tank. From this tank, the water was pumped through a diatomaceous-earth filter and sent back to the wave tank through a port at the opposite end of the tank from the skimmers. When fresh water was needed, tap water was sent through a separate filter before entering the wave tank. The skimming system was run continuously as the measurements were being taken in order to maintain a low surfactant level.

### 2.2 Wave profile measurements

The wave crest profiles were measured with a photographic technique that employs a laser light sheet and a CCD camera (*Kodak Megaplus ES 1.0*) with image size of 1008 by 1018 pixels and a maximum frame rate of 30 Hz. The laser, light-sheet optics, and camera were mounted on the instrument carriage and moved along the tank with the breaking wave crest. The plane of the light sheet was oriented vertically along the centerline of the tank and the water was mixed with fluorescent dye. The camera viewed the intersection of the light sheet and the water surface from the side and recorded instantaneous images of the surface profile of the wave crest along the centerline of the tank. From each digital image, the surface profile was extracted with gradient-based edge detection techniques.

### 2.3 Mean flow measurements

A rake of three Pitot tubes was used for the mean velocity measurements in the wakes of the breakers. The rake had a spanwise horizontal spacing between tubes of 10 cm and a vertical spacing of 10 mm. The large horizontal spacing was chosen to minimize the interaction between the individual tubes. The rake was mounted to the instrument carriage via a linear traverser to allow vertical positioning. Each Pitot tube was connected through transparent Tygon tubing to a separate differential, diaphragm-type pressure transducer (*Validyne* Model P305D), each having a range of ±0.2 psi. The three pressure transducers were mounted on the instrument carriage. The analog voltage output of each pressure transducer was connected to a 12-bit analog-to-digital (A/D) converter operating at 300 samples per second and the digitized output was stored in the memory of a computer. The signal taken during the steady state part of each run was then averaged. Division of the full pressure range of the transducer by the resolution of the A/D converter yields an accuracy of 0.1 cm/s at an average speed equal to the towing speed, 80.4 cm/s. However, during runs made with the Pitot tubes moving through the undisturbed water in the towing tank, a pressure fluctuation corresponding to a root-mean-square velocity fluctuation of 0.2 cm/s was observed.
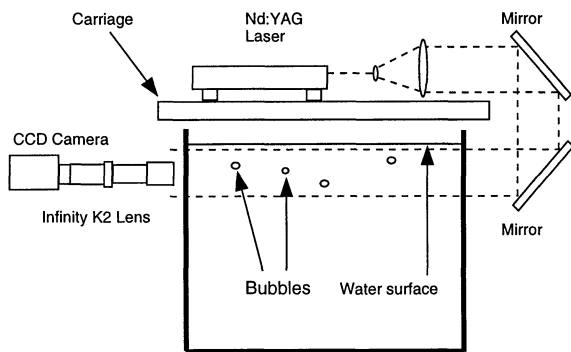
Figure 2. Schematic showing shadowgraph system used for bubble measurements.



Figure 3. Mean (top curves) and root-mean-square (bottom curves) surface height profiles for the weak and strong breakers: '– – – –' weak breaker, '————' strong breaker. The mean water level is at 70 mm and the flow in the reference frame of the crest is from left to right.

## 2.4 Bubble measurements

The shadowgraph optical system used to measure the bubbles is shown in Figure 2. This system is similar to that developed by Jähne and Geißler (1994). The light used for the imaging is created by a pulsed Nd:YAG laser. The laser head is mounted on the instrument carriage while the power supply remains on the floor beside the tank. A long umbilical allows the laser head to move freely down the tank with the instrument carriage. The laser produces 0.5 $\mu s$ pulses of green light (532 nm wavelength) with an energy of 12 mJ per pulse. Upon emission from the laser head the light is diffused by an opal filter which significantly reduces both the coherence and the intensity of the light. The light is then directed through two achromatic doublet lenses which expand and collimate the beam. These two lenses are separated by a distance equal to the sum of their focal lengths. A periscope consisting of two mirrors tilted 45° from the horizontal in contrary directions sends the beam through the tank perpendicular to the glass side walls. After passing through the tank horizontally, the light enters an *Infinity K2 Telescopic Microscope* lens and then a CCD camera. The lens is focused on the vertical center plane of the wave tank. The camera (*Kodak Megaplus ES 1.0*) is shuttered to capture 15 image pairs per second. A timing signal is produced by the camera at the beginning of each image pair. This signal is sent to a function generator which, in turn, sends two pulses to the trigger input of the laser. The time delays for the two pulses from the function generator are adjusted so that one light pulse occurs in each image with a time delay between the two pulses of 3$ms$.

Two calibration procedures were required for the shadowgraph system. First, to determine the relationship between number of pixels and physical distance, a ruler was placed in the focal plane located at the centerplane of the tank. By examination of an image of the ruler, the viewing area was found to be 23.5 mm by 23.5 mm (43.3 pixels/mm) for all measurements. Next, the effect of the depth of field of the camera-lens pair was determined. The laser back lighting for the photographs produces a white background while the bubbles appear as dark circular regions. Since the light source is nearly parallel, the image of a given bubble is nearly independent of the bubble's distance, $z$, from the camera lens. Bubbles that are positioned in the focal plane of the lens (the
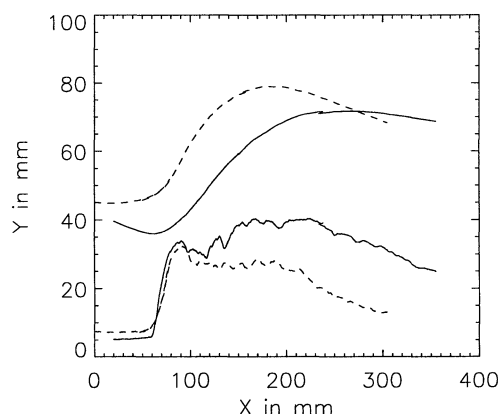
center plane of the tank, $z_0$) appear in the image as black circles with sharp edges. However, when the bubble position is not in the focal plane of the lens the resulting image is blurred. This effect is, of course, stronger for smaller bubbles and results in an effective measuring volume, $A_m \Delta z$ (where $A_m$ is the area covered by the image, 23.5 mm by 23.5 mm, and $\Delta z$ is the depth of focus about $z_0$). The following calibration procedure was performed to obtain a curve of $\Delta z$ versus bubble radius for the shadograph system. Targets for the calibration images consisted of a Patterson globe reticle with 7 black circles (dots) of varying diameter from 110 $\mu$ m to 450 $\mu$m and a set of spheres with diameters of 0.8 mm, 1.6 mm and 3.2 mm that were attached to a microscope slide. The calibration targets were mounted to a traverse system and images were taken with each target first at the focal plane and then at positions both closer to and further from the lens. When the target was far from the focal plane, the images of the dots or spheres began to blur resulting in lower average grey intensities and less sharp edges. The average intensity and radius of each dot or sphere was determined by fitting an axisymmetric function to the appropriate intensity pattern. By setting an average image intensity threshold, the values of $\Delta z$ for each diameter were obtained. This gave the desired relationship between the effective measurement volume and bubble radius. Further details of this procedure and a number of calibration plots can be found in Li et al. (1998).

## 3. RESULTS AND DISCUSSION

Measurements were obtained for two breaking waves that were generated with the same towing speed, $U_0 = 80.4$ cm/s, and angle of attack of the hydrofoil, 9°, but different foil depths, $d = 0.85c$ and $0.95c$. The breaking intensity increases as the foil is brought closer to the free surface; therefore, in the following the breakers generated with $d = 0.95c$
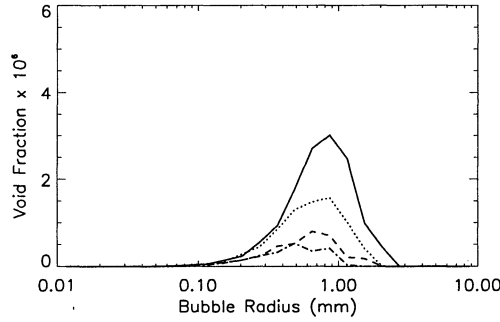
387

Figure 4. Void fraction versus bubble radius for the measurement window at the free surface for four streamwise locations: '————' $x = 0.6\lambda_0$, '········' $x = 0.8\lambda_0$, '————' $x = 1.0\lambda_0$, '—·—·—·—' $x = 1.2\lambda_0$. Weak breaker.



Figure 5. Void fraction versus bubble radius for the measurement window at the free surface for four streamwise locations: '————' $x = 0.6\lambda_0$, '········' $x = 0.8\lambda_0$, '————' $x = 1.0\lambda_0$, '—·—·—·—' $x = 1.2\lambda_0$. Strong breaker.

and $d = 0.85c$ are referred to as the weak and strong breakers, respectively. For these conditions, the Froude numbers based on $d$, $Fr_d$ ($= U_0/\sqrt{gd}$, where $g$ is the gravitational acceleration), were 0.619 and 0.586, respectively.

The results of the surface height profile measurements are given in Figure 3. Comparison of the mean profiles of the two waves indicates that both the troughs and crests of the strong breaker are located at a lower elevation than those of the weak breaker. However, in agreement with Duncan (1981), the height ($h_b$) as measured from the trough in front of the breaker to the crest is nearly the same for the two waves, 35.5 mm. This yields a Froude number $U_0/\sqrt{gh_b} = 1.36$ as compared to the value of 1.29 found by Duncan as an average of data from 12 different breakers. Note also that behind the crest the surface height of the weak breaker decreases more rapidly than that of the strong breaker. This is an indication that the following wavetrain of the weaker breaker has a larger amplitude than that of the strong breaker in agreement with the findings of Duncan (1981). The root-mean-square surface height fluctuation is on average larger for the stronger breaker.

Bubble measurements were obtained at four streamwise locations behind each breaker: $x = 0.6$, 0.8, 1.0, and 1.2$\lambda_0$, where $\lambda_0$ ($= 2\pi U_0^2/g$) is the length of a linear wave with phase speed equal to the towing speed. For each streamwise location, the measurements were taken at two vertical locations with the centers of the images located 6.5 mm and 30 mm below the free surface. A total of about 30 image pairs was taken during each experimental run and about 10 runs were performed for each measurement position. From each image pair, the radius, position, and velocity of each bubble was measured. The depth of field calibration data described in the previous section was used with the bubble data to obtain various measurements of the bubble population that are based on total measurement volume. The bubble velocities were determined from each frame pair by measuring the frame-to-frame displacements of each bubble.

Figure 4 and Figure 5 show the distributions of void fraction with bubble radius, $r$, in the top measurement window for the four streamwise locations for the weak and strong breakers, respectively. At a given $x/\lambda_0$, the total void fraction is
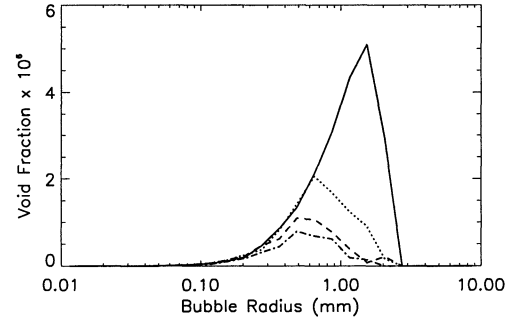
larger for the stronger breaker. Since air bubbles enter the flow in the turbulent breaking zone and the root-mean-square surface height fluctuation is larger for the stronger breaker, it is not surprising to find larger void fractions for this wave. As $x/\lambda_0$ increases, both the total void fraction and the bubble radius at the peak in the void fraction, $r_{max}$, decrease. These results probably indicate that the larger bubbles are leaving the measurement window through the free surface. The vertical distributions of void fraction for the weak and strong breakers are given in Figures 6 and 7, respectively. At all measurement locations there is a peak void fraction located between about 10 mm and 20 mm below the free surface and, from there, the void fraction tends to zero as either the depth increases or the free surface is approached. The void fractions and the depths of the void fraction peak are generally larger for the stronger breaker.

The horizontal components of the mean bubble and fluid velocities are plotted versus depth in Figures 8 and 9 for the weak and strong breakers, respectively. The curve for the water velocity was obtained by fitting the function

$$U(z) = U_0\left[1 - q\frac{1 - \tanh(a_1 z^2 + a_2)}{1 - \tanh(a_2)}\right] \qquad (1)$$

to the measured data $U(z)$, where $a_1$ and $a_2$ are fitting parameters, $z$ is the vertical coordinate with $z = 0$ at the free surface, and

$$q = \frac{U_0 - U(0)}{U_0}. \qquad (2)$$

The best set of constants ($U(0)$, $a_1$ and $a_2$) for the given velocity data set were determined by minimizing the sum of the squared deviations. (This function was used by Triantafyllou et al. (1986) to fit the data in the near wake of a cylinder.) The mean water velocity data shows behavior typical of a wake flow with the wake centerline at the free surface. The surface velocity is lower and the wake thickness is greater for
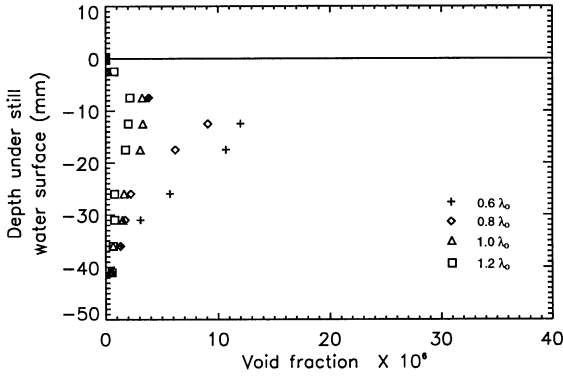
Figure 6. Void fraction versus depth below the free surface at four streamwise locations behind the weak breaking wave, $d/c = 0.95$.
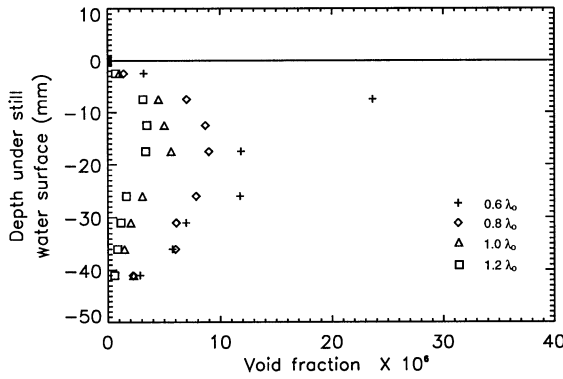


Figure 7. Void fraction versus depth below the free surface at four streamwise locations behind the strong breaking wave, $d/c = 0.85$.



Figure 8. Horizontal component of mean fluid and bubble velocities versus depth below the water surface for the strong breaker, $x = 1.0\lambda_0$: '+' bubble velocity data, '——' water velocity.



Figure 9. Horizontal component of mean fluid and bubble velocities versus depth below the water surface for the weak breaker, $x = 1.0\lambda_0$: '+' bubble velocity data, '——' water velocity.

the stronger breaker indicating that the wake of this wave has a larger momentum deficit. Near the free surface, the bubble velocities and the water velocities are nearly equal (except for the bubble velocity data point closest to the surface in the weak breaker case). However, at the depth of the mean shear layer in the water velocity profile, the bubble velocities are much less than those of the water. These lower bubble velocities are probably an indication that the bubbles travel preferentially in regions of slow moving fluid, probably at the cores of vortex structures.

The distributions of the vertical component of the mean bubble velocity versus bubble radius is given in Figures 10 and 11 for the weak and strong breakers, respectively. Curves are given for each of the four streamwise measurement locations. In all cases, the vertical velocity increases with increasing bubble radius and reaches values as high as 23 cm/s at about a 1 or 2 mm radius. For isolated bubbles rising in a quiescent fluid, the distribution of vertical velocity has a peak value (Harper, 1972). Maxworthy et al. (1996) found this peak
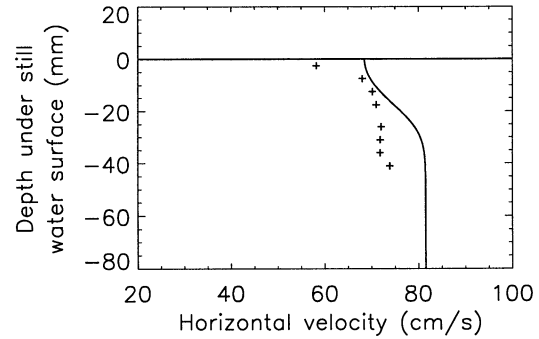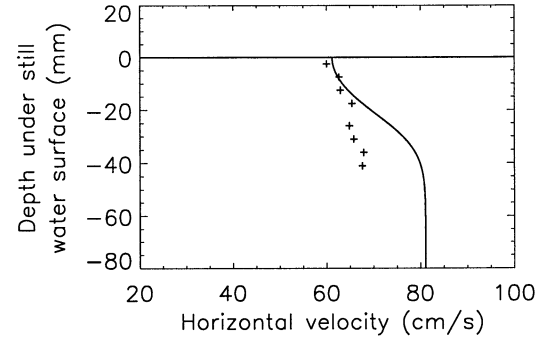
value to equal 0.35 m/s and to occur at a bubble radius of 0.75 mm. The vertical velocities in the present data set at any bubble radius are less than those measured by Maxworthy et al. (1996).

## 4. CONCLUSIONS

The surface height fluctuations at the crest, vertical distribution of mean horizontal water velocity in the wake, and the radii, spatial distributions, and velocities of bubbles in the wake were measured for two steady breakers with the same phase speed but different breaking intensities. The root-mean-square surface height fluctuation on the forward face of the breaking wave crest and the wake void fraction at the same location behind the two breakers were higher for the stronger breaker than for the weaker breaker. The vertical distribution of void fraction in the wake was found to have a peak at depths on the order of 1 to 2 cm below the free surface. The
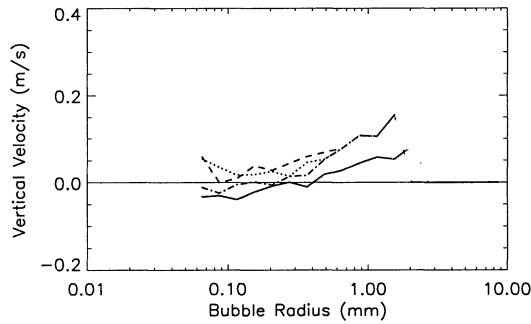
389

Figure 10. Vertical component of mean velocity of bubbles versus bubble radius at four streamwise locations: '————' $x = 0.6\lambda_0$, '········' $x = 0.8\lambda_0$, '— — — —' $x = 1.0\lambda_0$, '— · — · —' $x = 1.2\lambda_0$. Weak breaker.
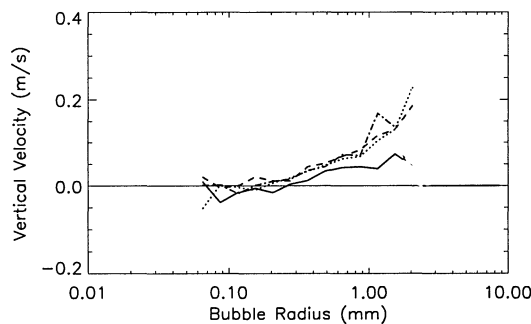


Figure 11. Vertical component of mean velocity of bubbles versus bubble radius at four streamwise locations: '————' $x = 0.6\lambda_0$, '········' $x = 0.8\lambda_0$, '— — — —' $x = 1.0\lambda_0$, '— · — · —' $x = 1.2\lambda_0$. Strong breaker.

total void fraction decreased with streamwise distance behind the breaker as did the bubble radius at the peak in the radial distribution of void fraction. The mean vertical velocity of the bubbles increased with bubble radius and reached values as high as 23 cm/s at a radius of 1 to 2 mm. The above results are consistent with the idea that as the bubbles travel along in the wake the larger bubbles continually leave the flow through the free surface. The vertical distribution of mean horizontal bubble velocity was about equal to the mean horizontal water velocity near the free surface, but was lower than the water velocity in the region of the wake shear layer.

## ACKNOWLEDGEMENTS

## REFERENCES

Battjes, J. A. and Sakai, T. 1981 "Velocity Field in a Steady Breaker," Journal of Fluid Mechanics, Vol. 111, pp. 421-437.

Duncan, J. H. 1981 "An Experimental Investigation of Breaking Waves Produced by a Towed Hydrofoil" Proc. R. Soc. Lond., Vol. 377, pp. 331-348

Duncan, J. H. 1983 "The Breaking and Nonbreaking Wave Resistance of a Two-Dimensional Hydrofoil," Journal of Fluid Mechanics , Vol. 126, pp. 507-520.

Harper, J. F. 1972 "The Motion of Bubbles and Drops Through Liquids" Advances in Applied Mechanics, Vol. 12, pp. 59-129

Jähne, B. and Geißler, P. 1994 Proc. Conf. on Computer Vision and Pattern Recognition, Seattle, 20-23 June.

Li, C. Y., Miller, M. P. and Duncan, J. H. 1998 "Air Entrainment in Steady Breaking Waves," presented at the ASME Fluids Engineering Summer Meeting, Washingtion D.C, June, 1998.

Maxworthy, T., Gnann, C., Kurten, M. and Durst, F. 1996, "Experiments on the rise of air bubbles in clean viscous liquids," Journal of Fluid Mechanics, Vol. 321, pp. 421-441.

Poorte, R. E. G. 1998 "On the motion of bubbles in active grid generated turbulent flows," Dissertation, University of Tweente.

Spelt, P. D. M. and Biesheuvel, A. 1997 "On the motion of gas bubbles in homogeneous isotropic turbulence," Journal of Fluid Mechanics, Vol. 336, pp. 221-244.

Triantafyllou, G. S., M. S. Triantafyllou, and C. Chrysostomidis 1986 "On the formation of vortex streets behind stationary cylinders," Journal of Fluid Mechanics, Vol. 170, pp. 461-477.